Dalton Transactions

ROYAL SOCIETY OF CHEMISTRY

PAPER

View Article Online
View Journal | View Issue

Cite this: *Dalton Trans.*, 2025, **54**, 17250

Bimetallic Ru/Co nanoparticles stabilized by N-heterocyclic carbenes as catalysts for H/D exchange in N-heterocycles with deuterium gas

Pablo Molinillo,†[a] Ana Gálvez del Postigo,†[a] Maxime Puyo,[a] Florencia Vattier,[a] Bertrand Lacroix,[b] Nuria Rendón,*[a] Patricia Lara*[a] and Andrés Suárez*[a]

Received 18th August 2025,
Accepted 3rd November 2025

DOI: 10.1039/d5dt01969a

rsc.li/dalton

A series of bimetallic ruthenium/cobalt nanoparticles (**RuCo·IMes**) stabilized with a N-heterocyclic carbene ligand, 1,3-bis(2,4,6-trimethylphenyl)imidazol-2-ylidene (IMes), was prepared through co-decomposition of the Ru(COD)(COT) (COD = 1,5-cyclooctadiene; COT = 1,3,5-cyclooctatriene) and Co(COD)(η^3-cyclooctenyl) precursors with H_2 (3 bar) using ligand/metal ratios of 0.2. The resulting nanoparticles, which exhibit mean sizes between 1.1 and 1.6 nm, were characterized using (high) transmission electron microscopy (TEM, HRTEM), inductively coupled plasma (ICP) analysis and X-ray photoelectron spectroscopy (XPS). Particularly, XPS measurements support the presence of both Co and Ru atoms on the nanoparticle surfaces and the coordination of the IMes ligand. Finally, the **RuCo·IMes** nanoparticles were applied to the hydrogen isotope exchange (HIE) reactions with deuterium gas (D_2) in N-heterocycles. The catalytic activity and deuterium incorporation selectivity of the **RuCo·IMes** nanoparticles were found to strongly depend on the specific substrate examined, generally providing lower activities and slightly higher selectivities with the presence of increasing amounts of Co in the nanoparticles.

Introduction

Hydrogen isotope labeling of organic compounds has gained great attention as deuterium- and tritium-enriched molecules are being more frequently used in drug discovery and development, clinical analysis, chemical and biochemical reaction mechanistic investigations and the synthesis of pharmaceutical compounds with improved pharmacokinetic profiles and bioavailability.[1] In order to obtain deuterium-enriched molecules, hydrogen isotope exchange (HIE) reactions using deuterium gas provide a particularly desirable methodology since it allows the installation of hydrogen heavier isotopes at a late synthetic stage through direct H/D exchange.[2–7] In this context, metal nanoparticles (NPs) have been shown to efficiently promote the activation of C–H and H–H bonds under mild conditions,[8] and consequently these nanosystems are receiving an increasing attention as HIE catalysts.[9–28] The use of metal nanoparticles in HIE is advantageous in comparison to metal based homogeneous and heterogeneous catalytic systems. Metal complexes usually promote moderate isotope incorporation with high selectivity at specific positions; meanwhile, heterogeneous catalysts give rise to high H/D replacement but with reduced selectivity and often under relatively harsh conditions. Colloidal systems combine advantages associated to both homogeneous and heterogeneous systems.

Due to the high prevalence of N-heteroarene moieties in molecules exhibiting biological and pharmaceutical properties,[29] hydrogen heavier isotopes labelling of these derivatives is an important transformation. However, use of D_2 as deuterium source might lead to the reductive deuteration of the heteroaromatic scaffolds. For instance, although Ru nanoparticles have been shown to efficiently deuterate N-heteroarenes,[11,15,16] amines,[11] amino acids,[12,13,17] and phosphorus-containing molecules,[14,27] as well as performing HIE in derivatives containing E–H (E = B, Si, Ge, Sn) bonds,[28] nanocatalysts based on this metal also catalyze the hydrogenation of (hetero)aromatic molecular fragments.[11,17,24,27,30] Another drawback to circumvent is the limited regioselectivity provided by Ru-based colloidal systems in H/D replacement as deuterium incorporation usually occurs at multiple sites. In this regard, a potential strategy for controlling the reactivity of HIE catalysts resides in the use of capping ligands such as

---

[a] *Instituto de Investigaciones Químicas (IIQ), Departamento de Química Inorgánica, and Centro de Innovación en Química Avanzada (ORFEO-CINQA). CSIC and Universidad de Sevilla, Avda. Américo Vespucio, 49, 41092 Sevilla, Spain. E-mail: nuria@iiq.csic.es, patricia@iiq.csic.es, andres.suarez@iiq.csic.es*
[b] *Departamento de Física Aplicada I, Escuela Politécnica Superior, Universidad de Sevilla, Virgen de África 7, 41011 Sevilla, Spain*

† These authors contributed equally.

N-heterocyclic carbenes (NHCs).[31] These derivatives are particularly interesting stabilizing agents due to their easy preparation, wide structural variability and strong donor properties, and their use as stabilizing agents facilitates the control of the size, shape and surface properties of the nanomaterials by simply changing the ligand structure and surface metal/ligand ratio.[32] Furthermore, additional control of the reactivity can be achieved by the addition of a second metallic element, thus leading to nanoparticles comprised of two different metals. These bimetallic nanocatalysts, particularly when composed of a noble metal and a first-row transition metal, have emerged as an important class of catalysts since they can provide enhanced catalytic activities and/or selectivities due to the occurrence of synergistic effects between the two metallic components.[33] In this context, bimetallic RuM (M = Pt, Ir, Ni) and PdNi nanoparticles stabilized by NHC ligands have recently been tested in HIE with D_2. Notably, while these systems have been examined in the deuteration of amino acids,[17,18,24,26] only RuIr nanoparticles have been studied for deuteration of an N-heterocyclic substrate, namely 2-phenylpyridine.[24]

Herein, we describe the synthesis and characterization of a series of small and monodispersed bimetallic nanoparticles composed of Ru and Co, a non-noble metal, which are stabilized by a N-heterocyclic carbene ligand, 1,3-bis(2,4,6-trimethylphenyl)imidazol-2-ylidene (IMes). Similarly, the impact of the nanoparticle metal composition on the catalytic activity and selectivity in the deuteration of a series of N-heterocycles using deuterium gas under mild conditions is examined. While RuCo nanoparticles have been employed in other catalytic processes,[34] to our knowledge, RuCo bimetallic nanocatalysts stabilized by NHC ligands and their applications to HIE reactions have not been previously investigated.

Results and discussion

Synthesis and characterization of RuCo·NHC nanoparticles

Bimetallic ruthenium/cobalt nanoparticles stabilized by IMes ligand were synthesized *via* co-decomposition of different ratios of Ru(COD)(COT) and Co(COD)(η^3-cyclooctenyl).[35] Thus, **$Ru_{50}Co_{50}$·IMes** nanoparticles were prepared by exposing to H_2 (3 bar) a 1 : 1 mixture of Ru(COD)(COT) and Co(COD)(η^3-cyclooctenyl) dissolved in THF, in the presence of substoichiometric amounts of IMes (ligand/metal ratio = 0.2) (Scheme 1). The obtained nanoparticles exhibit small mean sizes of 1.3 ± 0.4 nm, with narrow size distributions, as determined by TEM analysis (Fig. 1). Moreover, the nanoparticle metal content was determined by ICP analysis and fairly reproduces the theoretical 1 : 1 molar metal composition (Table 1). Similarly, nanomaterials having a cobalt enriched composition, **$Ru_{10}Co_{90}$·IMes**, and a small amount of the non-noble metal, **$Ru_{90}Co_{10}$·IMes**, were similarly prepared in order to determine the influence of the non-precious transition metal in the nanoparticles reactivity. Both nanomaterials also exhibit narrow size distributions and, as in the case of **$Ru_{50}Co_{50}$·IMes** nanoparticles, are stable both in solution and in the solid state under inert atmosphere over prolonged periods of time

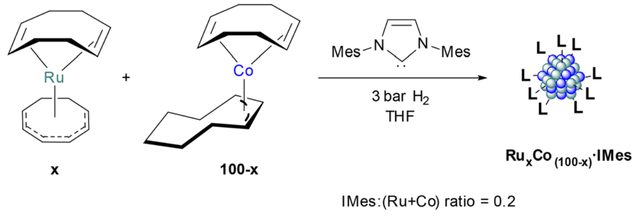

Scheme 1 Synthesis of **RuCo·IMes** nanoparticles.

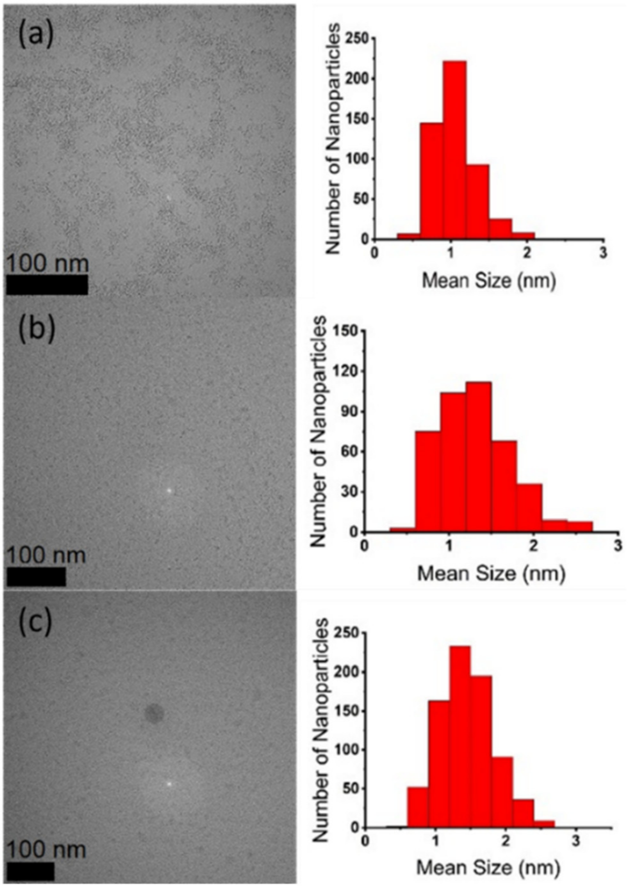

Fig. 1 TEM images with size distribution histograms of (a) **$Ru_{90}Co_{10}$·IMes**, (b) **$Ru_{50}Co_{50}$·IMes** and (c) **$Ru_{10}Co_{90}$·IMes**.

Table 1 TEM and ICP analyses of the **Ru·IMes** and **RuCo·IMes** nanoparticles

Nanoparticles	%wt Ru[a]	%wt Co[a]	Mean size[b] (nm)
Ru·IMes[c]	66	—	1.5 (0.3)
$Ru_{90}Co_{10}$·IMes	36	2	1.1 (0.3)
$Ru_{50}Co_{50}$·IMes	17	14	1.3 (0.4)
$Ru_{10}Co_{90}$·IMes	5	19	1.6 (0.5)

[a] %wt Ru and Co content as determined by ICP analysis. [b] Measured from TEM images. Standard deviations in parentheses. [c] Ref. 28 and 36.

(several weeks). Also, for the sake of comparison, single metal **Ru·IMes** (1.5 nm) nanoparticles were synthesized following an analogous procedure using a IMes/Ru ratio of 0.2, as previously reported.[28,36]

High-resolution transmission electron microscopy (HRTEM) was conducted to evaluate the crystalline structure of the **RuCo·IMes** nanoparticles. Fig. 2 shows the most representative HRTEM micrographs obtained for these nanomaterials, along with the corresponding digital diffraction patterns (DDPs). For **$Ru_{90}Co_{10}$·IMes** nanoparticles, the measured spacings (0.204 nm and 0.212 nm) and angles (73°) between the interference fringes determined on the Fast Fourier Transform (FFT) closely align with those of (101) and (002) planes of the hexagonal closed packed (hcp) ruthenium structure (d_{101} = 0.205 nm; d_{002} = 0.214 nm, ((101), (002)) = 61°) (Fig. 2a).[37] Note that the measured spacings could also correspond to the (002) and (100) crystallographic planes of hcp cobalt structure,[38] however the angle between these planes would be 90°, far from the angle measured on the FFT. This observation therefore indicates that the **$Ru_{90}Co_{10}$·IMes** nanoparticles present a dominant hcp Ru structure in agreement with their composition. In the case of **$Ru_{10}Co_{90}$·IMes** nanoparticles, the observed fringes show the same spacings (0.217 nm) and angle (90°) that match the (100) and (010) planes of the hcp Co structure (d_{100} = 0.217 nm),[38] which turns out to be dominant in this case, also in agreement with their composition (Fig. 2b). Finally, HRTEM of **$Ru_{50}Co_{50}$·IMes** nanoparticles reveals fringes with the same spacings (0.215 nm) and an angle of 74° that are incompatible with the hcp structures of Ru and Co, suggesting a nanoalloy composition for this material (Fig. 2c).

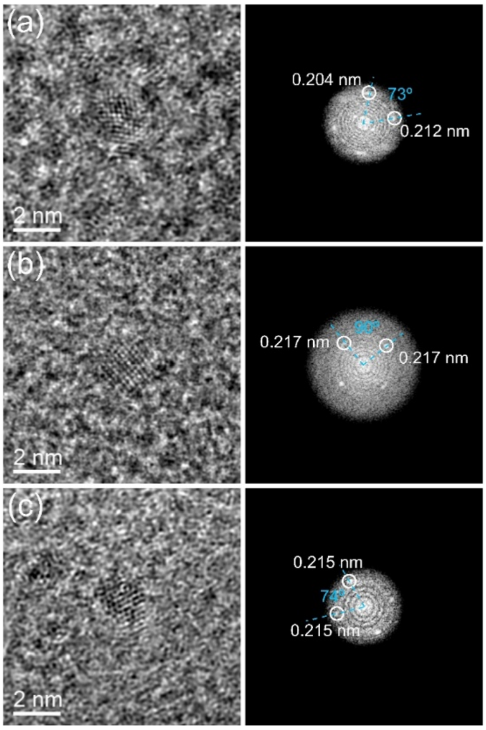

Fig. 2 HRTEM micrographs (left) with their corresponding DDPs (right) for (a) **$Ru_{90}Co_{10}$·IMes**, (b) **$Ru_{10}Co_{90}$·IMes** and (c) **$Ru_{50}Co_{50}$·IMes** nanoparticles.

The bimetallic nature of the nanoparticles was further investigated through XPS measurements. The XPS spectrum of the **$Ru_{50}Co_{50}$·IMes** sample shows two signals centred at 796.1 and 780.7 eV binding energy (BE), corresponding to the Co $2p_{1/2}$ and Co $2p_{3/2}$ peaks, respectively. The high-resolution spectrum of the Co $2p_{3/2}$ peak exhibits a complex structure due to the presence of metallic and oxidized cobalt species, which display significant multiplet splitting (Fig. 3, bottom). The oxidized cobalt species likely originate from sample handling during XPS measurements. Deconvolution of these peaks enables quantification of the content of Co(0), whose signal appears at 777.8 eV BE and makes up to 15% of the total.[39] Similar results were obtained from the XPS analysis of **$Ru_{10}Co_{90}$·IMes** nanoparticles. In this case, the Co $2p_{1/2}$ and Co $2p_{3/2}$ peaks appear at 796.4 and 780.6 eV, respectively. The peak corresponding to zero-oxidation-state cobalt in the Co $2p_{3/2}$ signal fitting appears at 779.0 eV, being 10–15% of the total cobalt amount (Fig. 3, top). The oxidized material was restricted to only a few atomic layers, as it was easily removed from the sample by mild Ar^+ sputtering during the XPS measurement (see Fig. S1).

Since the main photoemission peak for ruthenium, the Ru 3d signal, lies very close and partially overlaps with the C 1s peak due to the high carbon content of the nanoparticles, the Ru 3p signal was selected to analyze the ruthenium presence in the samples.[40] The Ru 3p region of the **$Ru_{50}Co_{50}$·IMes** nanoparticles appears as two signals centred at 484.6 and 462.3 eV, corresponding to the Ru $3p_{1/2}$ and Ru $3p_{3/2}$ peaks, respectively (Fig. 4a, bottom). The value of the spin orbit splitting was 22.2 eV, which is a typical value for Ru in zero oxidation-state.[28,41] Similarly, the XPS spectrum for the **$Ru_{10}Co_{90}$·IMes**

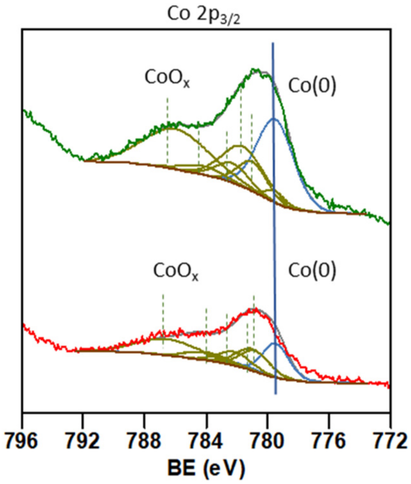

Fig. 3 Experimental and fitted high-resolution spectra of Co $2p_{3/2}$ region for **$Ru_{50}Co_{50}$·IMes** (bottom), and **$Ru_{10}Co_{90}$·IMes** (top). [Blue line: metallic Co; olive lines: main photoemissions and multiplet splitting peaks for CoO_x species (x = 1–1.5)].

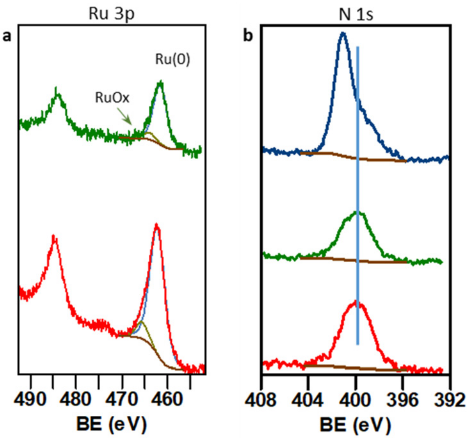

Fig. 4 (a) Experimental and fitted Ru 3p X-ray photoelectron spectral region for **$Ru_{50}Co_{50}$·IMes** (bottom), and **$Ru_{10}Co_{90}$·IMes** (top). (b) High resolution XPS spectra of N 1s region for **$Ru_{50}Co_{50}$·IMes** (bottom) and **$Ru_{10}Co_{90}$·IMes** (middle) nanoparticles, and free IMes ligand (top).

material shows the Ru 3p peaks at 484.0 and 461.7 eV for Ru $3p_{1/2}$ and Ru $3p_{3/2}$, respectively (Fig. 4a, top). The Ru $3p_{3/2}$ signals were well-fitted into two components at 461.9 and 464.5 eV for **$Ru_{50}Co_{50}$·IMes** (Fig. 4a, bottom), and at 461.6 and 463.9 eV for **$Ru_{10}Co_{90}$·IMes** (Fig. 4a, top), corresponding the lower value to metallic Ru and the higher to RuO_x species, resulting from the partial oxidation of the surface (approximately 8% in both samples).[28,41]

The XPS spectra of the nanoparticles also confirm the presence of the carbene ligand on the surface of the nanoparticles (Fig. 4b). The nitrogen atoms of the ligand produce a broad signal at 399.7 eV (fwhm 3.0 eV) for the **$Ru_{50}Co_{50}$·IMes** nanomaterial, and at 400.0 eV (fwhm 3.0 eV) in the case of the **$Ru_{10}Co_{90}$·IMes** nanoparticles, whereas in the free ligand the corresponding peak is detected at 401.0 eV (fwhm 3.1 eV).[28,42] Peak broadening toward lower BE values likely results from measurement-induced molecular degradation.

Table 2 presents the quantification in % atomic concentration on the nanoparticle surfaces obtained by integration of the peak areas in the spectra. Notably, the ratio of the carbene ligand to the two metals was very similar in both cases, with values of IMes/(Co + Ru) = 0.45–0.48. This value depends on two factors, the degree of coating and the size of the nanoparticles. Since the size is very similar for both nanoparticles, it might be concluded that the same coverage degree is achieved in both cases despite the different metal stoichiometries used. Moreover, the quantification of the two metals (in % atomic concentration) on the analyzed surface indicates that the atomic ratio in the **$Ru_{50}Co_{50}$·IMes** nanoparticles was Ru : Co = 1.5 : 1 (60% Ru and 40% Co). The spectra obtained at different sample tilting angles with respect to the analyzer (15°, 30°, and 60° take-off) revealed that the metal ratio remains homogeneous throughout the outer layers of atoms of the nanoparticles. Interestingly, this ratio differs from that obtained by ICP analysis, indicating a slight enrichment of cobalt in the internal composition. A similar analysis for the **$Ru_{10}Co_{90}$·IMes** nanoparticles revealed that the Ru : Co ratio was 0.17 : 1 (15% Ru and 85% Co).

Table 2 Quantitative analysis of the surface composition for **$Ru_{50}Co_{50}$·IMes** and **$Ru_{10}Co_{90}$·IMes** nanoparticles (percentage of atomic concentration %at)

Nanoparticles	Ru (%at)	Co (%at)	N (%at)	%Ru : %Co	IMes/ (Co + Ru)
$Ru_{50}Co_{50}$·IMes	30.8	20.2	49.0	60 : 40	0.48
$Ru_{10}Co_{90}$·IMes	7.8	44.5	47.7	15 : 85	0.45

Catalytic H/D exchange

The novel **RuCo·IMes** nanoparticles were examined in the H/D exchange with D_2 in nitrogen-containing heterocycles. Initial tests for catalyst performance comparison were carried out using 2-phenylpyridine (**S-1**) and D_2 (2 bar) in THF at 55 °C, with 5.0 mol% metal catalyst loadings (Table 3; see experimental section for details). The examination of 2-phenylpyridine as a model substrate allowed us to evaluate the selectivity of the HIE process with respect to reductive deuteration of the phenyl substituent, as well as to determine the influence of the pyridine fragment as directing group. Under the specified conditions, the cobalt-enriched **$Ru_{10}Co_{90}$·IMes** nanoparticles did not exhibit catalytic activity in neither H/D exchange nor reduction of **S-1**. Interestingly, increasing the amount of Ru in the nanoparticles using **$Ru_{50}Co_{50}$·IMes** predominantly produced the H/D exchange derivatives accompanied of minor amounts (<2%) of reduction by-products. Deuterium incorporation was mainly observed at the α position to the nitrogen

Table 3 H/D exchange in 2-phenylpyridine (**S-1**) catalyzed by **Ru·IMes** and **RuCo·IMes** nanoparticles[a]

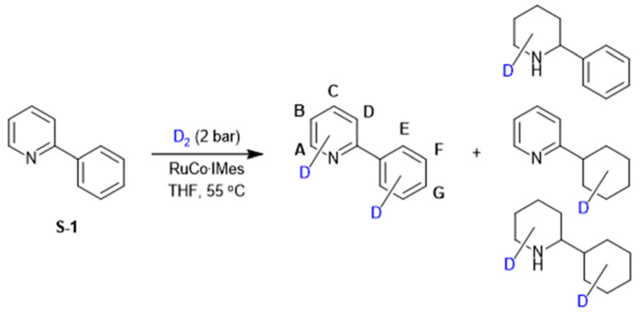

Nanoparticles	Red. (%)	A	B	C + D	E	F
Ru·IMes	66	83	26	30	88	10
$Ru_{90}Co_{10}$·IMes	55	90	13	31	93	13
$Ru_{50}Co_{50}$·IMes[b]	<2	60	2	5	17	0
$Ru_{10}Co_{90}$·IMes	0	0	0	0	0	0

[a] **A–F** positions refer to the non-reduced product (see reaction scheme). Reaction conditions, unless otherwise noted: 5.0 mol% metal loading, 2 bar D_2 (*ca.* 10 equiv.), 55 °C, THF. [*S*] = 0.15 M. Reaction time: 24 h. Deuterium incorporation as determined by ^{1}H NMR spectroscopy using an internal standard. H/D exchange selectivity determined by ^{2}H NMR spectroscopy. Deuterium incorporation at the G position was not observed. [b] Reaction time: 48 h.

atom of the pyridine ring (60% D enrichment), along with moderate labelling of the remote positions of the pyridine fragment (less than 5%) and the position E of the aryl substituent (17% D incorporation). Upon using bimetallic Ru-enriched **$Ru_{90}Co_{10}$·IMes** or **Ru·IMes** nanoparticles, a higher activity towards H/D exchange was determined, accompanied of a decrease of the deuteration selectivity in the position adjacent to the N atom (A) with respect to the *ortho* C–H site of the phenyl ring (position E). Moreover, significant substrate reduction is observed with these catalysts. This observation is in line with previously reported studies regarding the deuteration of 2-phenylpyridine with deuterium gas using monometallic Ru·NHC (NHC = N-heterocyclic carbene ligand) and bimetallic Ru_xIr_{100-x}·IMes nanoparticles, where Ru enriched nanoparticles gave rise to significant reduction of **S-1**.[22,24]

Encouraged by the observed influence of the metal composition of the **RuCo·IMes** nanoparticles in the chemoselectivity of the reaction of 2-phenylpyridine with D_2, we turned our attention to the deuteration of other pyridine containing molecule, 2,2′-bipyridyl (**S-2**). Reactions of **S-2** with D_2, performed under the same conditions previously employed in the HIE of **S-1**, did not show the formation of reduction products with the **Ru·IMes** nanoparticles (Table 4). Interestingly, the **$Ru_{90}Co_{10}$·IMes** nanoparticles were found to be more selective than the **Ru·IMes** catalyst since they provided similar deuterium incorporation at the position A, whereas lower levels of H/D exchange at the other positions were observed. In the case of **S-2**, the Co-enriched **$Ru_{50}Co_{50}$·IMes** and **$Ru_{10}Co_{90}$·IMes** nanoparticles were found to be inactive in the hydrogen isotope incorporation reaction.

2-Methylquinoline (**S-3**), an easily reducible N-heterocycle, was next chosen for catalyst comparison (Table 5). While complete heteroarene reduction was attained with the monometallic **Ru·IMes** colloid, the use of the **$Ru_{90}Co_{10}$·IMes** and **$Ru_{50}Co_{50}$·IMes** nanomaterials led to the formation of lower amounts of hydrogenated products. Moreover, the **$Ru_{90}Co_{10}$·IMes** catalyst was found to exhibit a higher selectivity towards the H/D exchange at the position A than the **$Ru_{50}Co_{50}$·IMes** nanoparticles. As in the case of substrates **S-1** and **S-2**, negligible catalytic activity was observed for the **$Ru_{10}Co_{90}$·IMes** nanomaterial.

Table 5 H/D exchange in 2-methylquinoline (**S-3**) catalyzed by **Ru·IMes** and **RuCo·IMes** nanoparticles[a]

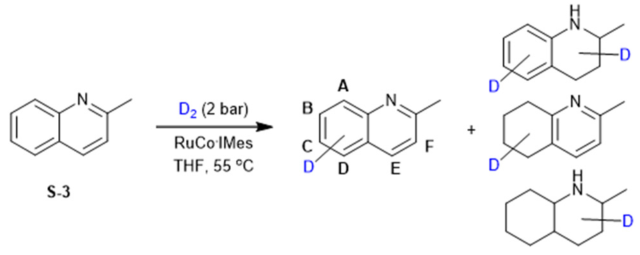

Nanoparticles	Red. (%)	A	B	C	E	F
Ru·IMes	>99	—	—	—	—	—
$Ru_{90}Co_{10}$·IMes	85	91	0	11	16	0
$Ru_{50}Co_{50}$·IMes [b]	75	92	15	13	58	2
$Ru_{10}Co_{90}$·IMes	0	0	0	0	0	0

[a] **A–F** positions refer to the non-reduced product (see reaction scheme). Reaction conditions, unless otherwise noted: 5.0 mol% metal loading, 2 bar D_2 (*ca.* 10 equiv.), 55 °C, THF. [*S*] = 0.15 M. Reaction time: 24 h. Deuterium incorporation as determined by ^1H NMR spectroscopy using an internal standard. H/D exchange selectivity determined by ^2H NMR spectroscopy. Deuterium incorporation at the D position was not observed. [b] Reaction time: 48 h.

Imidazole (**S-4**) was not reduced under the specified reaction conditions using the **Ru·IMes** nanoparticles and, high deuterium incorporation was detected at both positions A and B (Table 6). Interestingly, the **$Ru_{90}Co_{10}$·IMes** and **$Ru_{50}Co_{50}$·IMes** colloids also led to H/D exchange in high yields at these positions, whereas no reaction was observed in the case of the **$Ru_{10}Co_{90}$·IMes** nanoparticles. Post-catalysis TEM

Table 4 H/D exchange in 2,2′-bipyridyl (**S-2**) catalyzed by **Ru·IMes** and **RuCo·IMes** nanoparticles[a]

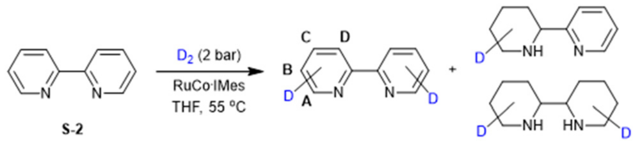

Nanoparticles	Red. (%)	A	B	C	D
Ru·IMes	0	96	88	79	61
$Ru_{90}Co_{10}$·IMes	0	95	45	38	21
$Ru_{50}Co_{50}$·IMes [b]	0	0	0	0	0
$Ru_{10}Co_{90}$·IMes	0	0	0	0	0

[a] **A–D** positions refer to the non-reduced product (see reaction scheme). Reaction conditions, unless otherwise noted: 5.0 mol% metal loading, 2 bar D_2 (*ca.* 10 equiv.), 55 °C, THF. [*S*] = 0.15 M. Reaction time: 24 h. Deuterium incorporation as determined by ^1H NMR spectroscopy using an internal standard. H/D exchange selectivity determined by ^2H NMR spectroscopy. [b] Reaction time: 48 h.

Table 6 H/D exchange in imidazole (**S-4**) catalyzed by **Ru·IMes** and **RuCo·IMes** nanoparticles[a]

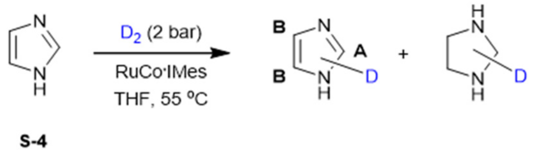

Nanoparticles	Red. (%)	A	B
Ru·IMes	0	98	98
$Ru_{90}Co_{10}$·IMes	0	98	97
$Ru_{50}Co_{50}$·IMes	0	98	95
$Ru_{10}Co_{90}$·IMes	0	0	0

[a] **A–B** positions refer to the non-reduced product (see reaction scheme). Reaction conditions, unless otherwise noted: 5.0 mol% metal loading, 2 bar D_2 (*ca.* 10 equiv.), 55 °C, THF. [*S*] = 0.15 M. Reaction time: 24 h. Deuterium incorporation as determined by ^1H NMR spectroscopy using an internal standard. H/D exchange selectivity determined by ^2H NMR spectroscopy.

Table 7 H/D exchange in benzoxazole (**S-5**) catalyzed by **Ru·IMes** and **RuCo·IMes** nanoparticles[a]

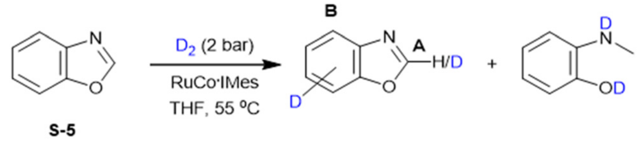

Nanoparticles	Red. (%)	A	B
Ru·IMes	59	96	59
$Ru_{90}Co_{10}$·IMes	30	69	8
$Ru_{50}Co_{50}$·IMes	0	14	3
$Ru_{10}Co_{90}$·IMes	0	0	0

[a] **A–B** positions refer to the non-reduced product (see reaction scheme). Reaction conditions, unless otherwise noted: 5.0 mol% metal loading, 2 bar D_2 (*ca.* 10 equiv.), 55 °C, THF. [*S*] = 0.15 M. Reaction time: 24 h. Deuterium incorporation as determined by ^1H NMR spectroscopy using an internal standard. H/D exchange selectivity determined by ^2H NMR spectroscopy. Deuterium incorporation at other positions was not observed. Reduction product was 2-(methylamino) phenol.

analysis of the **$Ru_{50}Co_{50}$·IMes** nanoparticles of the HIE reaction of **S-4** with D_2 revealed a slight increase of nanoparticle size 1.9 (0.4) nm (Fig. S2) in agreement with the preservation of the nanoparticle integrity after the reaction.

Lastly, HIE reactions of benzoxazole (**S-5**) with D_2 were examined (Table 7). While the **Ru·IMes** colloid provided high levels of deuteratium incorporation at the positions A and B, the reaction also produces the formation of significant amounts of 2-(methylamino)phenol (59%). The formation of this by-product is significantly suppressed by using the bimetallic nanoparticles. Thus, **$Ru_{90}Co_{10}$·IMes** nanoparticles gave rise to the reduction of **S-5** to 2-(methylamino)phenol with 30% yield, while the deuteration ratio between the positions A and B in the heteroarene increases to an A/B ratio of 8.6 : 1 from the 1.6 : 1 ratio provided by the **Ru·IMes** catalyst. Finally, a low activity in H/D exchange was attained with the **$Ru_{50}Co_{50}$·IMes** nanocatalyst.

Overall, the catalytic results indicate that RuCo nanoparticles stabilized by IMes exhibit increased chemoselectivity for deuterium incorporation into N-heterocycles, relative to reductive deuteration, as the Co content is increased. However, this enhanced selectivity is accompanied by a drastic decrease in nanoparticle reactivity.

Conclusions

In conclusion, the synthesis of narrowly dispersed bimetallic ruthenium/cobalt nanoparticles exhibiting small sizes have been achieved through the controlled decomposition of the corresponding Co and Ru organometallic complex precursors under H_2 in the presence of 0.2 equiv. of the IMes ligand. These nanomaterials have been extensively characterized by TEM, HRTEM, XPS and ICP analysis. Interestingly, as shown by the screening of a series of N-heterocycles, depending on the substrate, hydrogenation of aromatics was suppressed by increasing the non-noble/precious metal ratio in these nanomaterials. This comparative increase in H/D isotope exchange selectivity is generally accompanied by a reduction in catalytic activity, which is proposed to result from a dilution effect of catalytically active Ru centres upon alloy formation. Current research in our laboratory is directed to the use of other non-noble/precious metal combinations in the synthesis of bimetallic nanoparticles incorporating N-heterocyclic carbene ligands as stabilizing agents for applications in HIE reactions.

Experimental

General procedures and nanoparticles characterization techniques

All reactions and manipulations were performed under nitrogen or argon, either in a Braun Labmaster 100 glovebox or using standard Schlenk-type techniques. Solvents were distilled under nitrogen with the following desiccants: sodium benzophenone-ketyl for tetrahydrofuran (THF and THF-d_8) and sodium for pentane. Deuterium gas (99.8% D) was purchased from Sigma-Aldrich. 1,3-bis(2,4,6-Trimethylphenyl)imidazol-2-ylidene ligand (IMes),[43] and the Ru(COD)(COT)[44] and Co(COD) (η^3-cyclooctenyl)[45] metal precursors were prepared by previously reported methods. All the other chemicals were used as received from the commercial suppliers.

The morphology and size of the IMes-stabilized ruthenium/cobalt nanoparticles (**RuCo·IMes**) were determined by transmission electron microscopy (TEM) in a FEI TALOS F200S apparatus working at 200 kV at the Centro de Investigación, Tecnología e Innovación-CITIUS (Universidad de Sevilla). TEM samples were prepared taking a drop of the crude THF colloidal solution and depositing it over a covered holey copper grid. For the approximation of the particles mean size, *ca.* 300 particles were manually measured employing conventional TEM micrographs enlarged with ImageJ software. High-resolution transmission electron microscopy (HRTEM) images were recorded in a Thermo Scientific Talos F200X microscope at the Centro de Investigación, Tecnología e Innovación-CITIUS (Universidad de Sevilla) in order to assess the crystalline structure of the **RuCo·IMes** nanoparticles. TEM samples were analyzed under atmospheric conditions. An ABSF filter available within the "HRTEM filter" plugin was applied to enhance contrast by reducing the noise due to surrounding amorphous materials.

ICP analyses were performed at Mikroanalytisched Labor Pascher (Remagen, Germany).

X-ray photoelectron spectroscopy (XPS) experiments were performed in a PHOIBOS-100 spectrometer with a non-monochromatic Al-Kα radiation ($h\nu$ = 1486.6 eV) and a power source of 230 W. Samples were prepared in the glovebox and brought to the spectrometer under inert atmosphere to reduce nanoparticles exposure to air. However, samples insertion into the spectrometer were carried out under atmospheric conditions. The electron energy hemispherical analyzer was operated in the constant pass energy mode (SPECS PHOIBOS 100DLD). Low resolution survey spectra were obtained with a pass energy = 50 eV, while high energy resolution spectra of detected elements were obtained with a pass energy = 20 eV. The spectra were analyzed with the CASA XPS software, version 2.3.26.PR1.0 (Neal Fairly, UK). Shirley type backgrounds were used to determine the areas under the peaks. Convolution of peaks was made with GL(30) type shape lines for mixed oxide species and LA (50) for metallic core lines.

Liquid phase ^{1}H and ^{2}H NMR spectra were recorded on a Bruker DRX-400 spectrometer. Spectra were referenced to $SiMe_4$ (δ = 0 ppm) using the residual proton solvent peaks as internal standards. All NMR spectra were recorded at 25 °C.

Ruthenium/cobalt nanoparticles synthesis

For the preparation of the **$Ru_{50}Co_{50}$·IMes** nanoparticles, a solution of Ru(COD)(COT) (0.101 g, 0.32 mmol), Co(COD)(η^3-cyclooctenyl) (0.088 g, 0.32 mmol) and 1,3-bis(2,4,6-trimethylphenyl)imidazol-2-ylidene (0.039 g, 0.13 mmol) in freshly distilled THF (90 mL) were introduced in a Fisher-Porter vessel that was pressurized with 3 bar of H_2, and heated to 60 °C. The homogeneous solution, which turns black after approximately 1 h of reaction, was kept under stirring for 3 h. After this period of time, excess of H_2 was carefully released. The initial volume of solvent was reduced to *ca.* 5 mL under vacuum, 40 mL of pentane was added, and the colloidal suspension was cooled down to −50 °C. Solvent removal under reduced pressure allowed the isolation of a black solid, that was suspended in 40 mL of pentane and brought to dryness. This procedure was repeated three times (3 × 30 mL) in order to obtain a solid dark powder that was dried under vacuum (mass of isolated solid: 40 mg). The same procedure was also employed for the synthesis of the **$Ru_{90}Co_{10}$·IMes** (35 mg) and **$Ru_{10}Co_{90}$·IMes** (52 mg) nanoparticles by simply adjusting the initial Ru(COD)(COT)/Co(COD)(η^3-cyclooctenyl) ratio. For Ru and Co content determination by ICP and TEM analysis of the nanoparticles, see Table 1.

Representative procedure for H/D exchange with D_2 in N-heterocycles (Tables 3–7)

In a glovebox, a 25 mL Fisher-Porter vessel was charged with a solution of 2-phenylpyridine (**S-1**) (43 μL, 0.3 mmol) in THF (0.8 mL), 1.2 mL of a freshly prepared stock suspension of catalyst **$Ru_{50}Co_{50}$·IMes** (15 μmol metal) and hexamethylbenzene (4.0 mg, 0.025 mmol) in THF. The reactor was purged three times with D_2, and finally pressurized to 2 bar (*ca.* 20 equiv. D_2) and heated to 55 °C. After 24 h, the reactor was slowly cooled down to room temperature and depressurized. An aliquot of the reaction mixture was filtered through a short pad of Celite and brought to dryness. The conversion and selectivity were determined by ^{1}H and ^{2}H NMR spectroscopies, respectively.

Author contributions

P. M., A. G., M. P.: data curation, formal analysis, and investigation; F. V.: formal analysis (XPS), writing – review & editing; B. L.: formal analysis (HRTEM) and investigation; N. R., P. L., A. S.: conceptualization, data curation, formal analysis, investigation, methodology, visualization, writing – original draft, writing – review & editing.

Conflicts of interest

There are no conflicts to declare.

Data availability

The data supporting this article have been included as part of the manuscript, in the "Experimental" section, and in the supplementary information (SI). Supplementary information: XPS spectra after sputtering; TEM image after catalysis; NMR spectra of the catalytic reaction products. See DOI: https://doi.org/10.1039/d5dt01969a.

Acknowledgements

Financial support from MCIN/AEI/10.13039/501100011033/FEDER, UE (TED2021-129181B-I00 and PID2022-136570OB-I00), and VII PPIT-US/CITIUS is gratefully acknowledged. Parts of this work has also received funding from MICIN with funding from NextGenerationEU (PRTR-C17.I1) within the "Planes Complementarios con CCAA (Area of Green Hydrogen and Energy)" and it has been carried out in the CSIC Interdisciplinary Thematic Platform (PTI+) "Transición Energética Sostenible+ (PTI-TRANSENER+)".

References

1 (*a*) J. Atzrodt, V. Derdau, W. J. Kerr and M. Reid, *Angew. Chem., Int. Ed.*, 2018, **57**, 1758–1784; (*b*) A. Katsnelson, *Nat. Med.*, 2013, **19**, 656; (*c*) V. Derdau, C. S. Elmore, T. Hartung, B. McKillican, T. Mejuch, C. Rosenbaum and C. Wiebe, *Angew. Chem., Int. Ed.*, 2023, **62**, e202306019; (*d*) R. M. C. Di Martino, B. D. Maxwell and T. Pirali, *Nat. Rev. Drug Discovery*, 2023, **22**, 562–584; (*e*) T. G. Gant, *J. Med. Chem.*, 2014, **57**, 3595–3611; (*f*) T. Pirali, M. Serafini, S. Cargnin and A. A. Genazzani, *J. Med. Chem.*, 2019, **62**, 5276–5297; (*g*) L. Konermann, J. Pan and Y.-H. Liu, *Chem. Soc. Rev.*, 2011, **40**, 1224–1234; (*h*) T. Lavold, R. Zubarev and J. Astorga-Wells, in *Applied Biophysics for Drug Discovery*, ed. D. Huddler and E. R. Zartler, John Wiley & Sons, Inc., 2017; (*i*) W. D. Lehmann, *Mass Spectrom. Rev.*, 2017, **36**, 58–85; (*j*) M. Gómez-Gallego and M. A. Sierra, *Chem. Rev.*, 2011, **111**, 4857–4963; (*k*) E. M. Simmons and J. F. Hartwig, *Angew. Chem., Int. Ed.*, 2012, **51**, 3066–3072.

2 S. Kopf, V. Bourriquen, W. Li, H. Neumann, K. Junge and M. Beller, *Chem. Rev.*, 2022, **122**, 6634–6718.

3 J. Atzrodt, V. Derdau, W. J. Kerr and M. Reid, *Angew. Chem., Int. Ed.*, 2018, **57**, 3022–3047.

4 D. Zhao and T. Ritter, *Chem*, 2024, **10**, 3266–3267.

5 Q.-K. Kang and H. Shi, *Synlett*, 2022, 329–338.

6 G. Prakash, N. Paul, G. A. Oliver, D. B. Werz and D. Maiti, *Chem. Soc. Rev.*, 2022, **51**, 3123–3163.

7 X. Wang, Y.-B. Luo, Y.-X. Luo, M.-C. Liu, C.-H. Lu and R.-J. Song, *Appl. Organomet. Chem.*, 2024, **38**, e7602.

8 J. M. Asensio, D. Bouzouita, P. W. N. M. van Leeuwen and B. Chaudret, *Chem. Rev.*, 2020, **120**, 1042–1084.

9 M. Lepron, M. Daniel-Bertrand, G. Mencia, B. Chaudret, S. Feuillastre and G. Pieters, *Acc. Chem. Res.*, 2021, **54**, 1465–1480.

10 L. S. Ott, M. L. Cline, M. Deetlefs, K. R. Seddon and R. G. Finke, *J. Am. Chem. Soc.*, 2005, **127**, 5758–5759.

11 G. Pieters, C. Taglang, E. Bonnefille, T. Gutmann, C. Puente, J.-C. Berthet, C. Dugave, B. Chaudret and B. Rousseau, *Angew. Chem., Int. Ed.*, 2014, **53**, 230–234.

12 C. Taglang, L. M. Martínez-Prieto, I. del Rosal, L. Maron, R. Poteau, K. Philippot, B. Chaudret, S. Perato, A. Sam Lone, C. Puente, C. Dugave, B. Rousseau and G. Pieters, *Angew. Chem., Int. Ed.*, 2015, **54**, 10474–10477.

13 L. M. Martínez-Prieto, E. A. Baquero, G. Pieters, J. C. Flores, E. de Jesús, C. Nayral, F. Delpech, P. W. N. M. van Leeuwen, G. Lippens and B. Chaudret, *Chem. Commun.*, 2017, **53**, 5850–5853.

14 E. Bresó-Femenia, C. Godard, C. Claver, B. Chaudret and S. Castillón, *Chem. Commun.*, 2015, **51**, 16342–16345.

15 A. Palazzolo, S. Feuillastre, V. Pfeifer, S. Garcia-Argote, D. Bouzouita, S. Tricard, C. Chollet, E. Marcon, D.-A. Buisson, S. Cholet, F. Fenaille, G. Lippens, B. Chaudret and G. Pieters, *Angew. Chem., Int. Ed.*, 2019, **58**, 4891–4895.

16 V. Pfeifer, M. Certiat, D. Bouzouita, A. Palazzolo, S. Garcia-Argote, E. Marcon, D.-A. Buisson, P. Lesot, L. Maron, B. Chaudret, S. Tricard, I. del Rosal, R. Poteau, S. Feuillastre and G. Pieters, *Chem. – Eur. J.*, 2020, **26**, 4988–4996.

17 G. Mencia, P. Rouan, P.-F. Fazzini, H. Kulyk, V. Varela-Izquierdo, G. Lippens and B. Chaudret, *Catal. Sci. Technol.*, 2024, **14**, 4904–4911.

18 D. Bouzouita, G. Lippens, E. A. Baquero, P. F. Fazzini, G. Pieters, Y. Coppel, P. Lecante, S. Tricard, L. M. Martínez-Prieto and B. Chaudret, *Nanoscale*, 2019, **11**, 16544–16552.

19 M. Valero, D. Bouzouita, A. Palazzolo, J. Atzrodt, C. Dugave, S. Tricard, S. Feuillastre, G. Pieters, B. Chaudret and V. Derdau, *Angew. Chem., Int. Ed.*, 2020, **59**, 3517–3522.

20 M. Daniel-Bertrand, S. Garcia-Argote, A. Palazzolo, I. Mustieles Marin, P.-F. Fazzini, S. Tricard, B. Chaudret, V. Derdau, S. Feuillastre and G. Pieters, *Angew. Chem., Int. Ed.*, 2020, **59**, 21114–21120.

21 H. Kramp, R. Weck, M. Sandvoss, A. Sib, G. Mencia, P.-F. Fazzini, B. Chaudret and V. Derdau, *Angew. Chem., Int. Ed.*, 2023, **62**, e202308983.

22 D. Bouzouita, J. M. Asensio, V. Pfeifer, A. Palazzolo, P. Lecante, G. Pieters, S. Feuillastre, S. Tricard and B. Chaudret, *Nanoscale*, 2020, **12**, 15736–15742.

23 V. Pfeifer, T. Zeltner, C. Fackler, A. Kraemer, J. Thoma, A. Zeller and R. Kiesling, *Angew. Chem., Int. Ed.*, 2021, **60**, 26671–26676.

24 A. Zuluaga-Villamil, G. Mencia, J. M. Asensio, P.-F. Fazzini, E. A. Baquero and B. Chaudret, *Organometallics*, 2022, **41**, 3313–3319.

25 E. Levernier, K. Tatoueix, S. Garcia-Argote, V. Pfeifer, R. Kiesling, E. Gravel, S. Feuillastre and G. Pieters, *JACS Au*, 2022, **2**, 801–808.

26 O. Suárez-Riaño, G. Mencia, S. Tricard, J. Esvan, P.-F. Fazzini, B. Chaudret and E. A. Baquero, *Chem. Commun.*, 2023, **59**, 1062–1065.

27 F. Martinez-Espinar, A. Salom-Català, E. Bresó-Femenia, C. Claver, F. Baletto, J. M. Ricart, B. Chaudret, J. J. Carbó, C. Godard and S. Castillon, *Inorg. Chem.*, 2023, **62**, 4570–4580.

28 (*a*) P. Molinillo, M. Puyo, F. Vattier, B. Lacroix, N. Rendón, P. Lara and A. Suárez, *Nanoscale*, 2023, **15**, 14488–14495; (*b*) P. Molinillo, A. Gálvez del Postigo, M. Puyo, F. Vattier, A. M. Beltrán, N. Rendón, P. Lara and A. Suárez, *Inorg. Chem.*, 2025, **64**, 8125–8134.

29 E. Vitaku, D. T. Smith and J. T. Njardarson, *J. Med. Chem.*, 2014, **57**, 10257–10274.

30 (*a*) M. R. Axet and K. Philippot, *Chem. Rev.*, 2020, **120**, 1085–1145; (*b*) N. U. D. Reshi and A. G. Samuelson, *Appl. Catal., A*, 2020, **598**, 117561; (*c*) N. Romero, M. R. Axet and K. Philippot, *Adv. Catal.*, 2023, **72**, 115–157.

31 A. Palazzolo, T. Naret, M. Daniel-Bertrand, D. A. Buisson, S. Tricard, P. Lesot, Y. Coppel, B. Chaudret, S. Feuillastre and G. Pieters, *Angew. Chem., Int. Ed.*, 2020, **59**, 20879–20884.

32 (*a*) P. Lara and A. Suárez, *Top. Organomet. Chem.*, 2024, **75**, 133–198; (*b*) M. Ghosh and S. Khan, *ACS Catal.*, 2023, **13**, 9313–9325; (*c*) S. Wang, X. Yu, Y. Wang, B. Zhou, F. Shen and H. Cao, *Dalton Trans.*, 2024, **53**, 18440–18450; (*d*) Y. Y. An, J. G. Yu and Y. F. Han, *Chin. J. Chem.*, 2019, **37**, 76–87; (*e*) M. Koy, P. Bellotti, M. Das and F. Glorius, *Nat. Catal.*, 2021, **4**, 352–363; (*f*) H. Shen, G. Tian, Z. Xu, L. Wang, Q. Wu, Y. Zhang, B. K. Teo and N. Zheng, *Coord. Chem. Rev.*, 2022, **458**, 214425; (*g*) C. Cerezo-Navarrete, P. Lara and L. M. Martínez-Prieto, *Catalysts*, 2020, **10**, 1144; (*h*) C. A. Smith, M. R. Narouz, P. A. Lummis, I. Singh, A. Nazemi, C.-H. Li and C. M. Crudden, *Chem. Rev.*, 2019, **119**, 4986–5056.

33 (*a*) I. Mustieles Marin, J. M. Asensio and B. Chaudret, *ACS Nano*, 2021, **15**, 3550–3556; (*b*) Y. Nakaya and S. Furukawa, *Chem. Rev.*, 2023, **123**, 5859–5947; (*c*) S. Anand, D. Pinheiro and K. R. S. Devi, *Asian J. Org. Chem.*, 2021, **10**, 3068–3100; (*d*) L. Liu and A. Corma, *Chem. Rev.*, 2023, **123**, 4855–4933.

34 (*a*) V. Udumula, J. H. Tyler, D. A. Davis, H. Wang, M. R. Linford, P. S. Minson and D. J. Michaelis, *ACS Catal.*, 2015, **5**, 3457–3462; (*b*) H. Wang, C. Gao, R. Li, Z. Peng, J. Yang, J. Gao, Y. Yang, S. Li, B. Li and Z. Liu, *ACS Sustainable Chem. Eng.*, 2019, **7**, 18744–18752; (*c*) Z. Wei, Y. Liu, Z. Peng, H. Song, Z. Liu, B. Liu, B. Li, B. Yang and S. Lu, *ACS Sustainable Chem. Eng.*, 2019, **7**, 7014–7023; (*d*) D. Yu, P. Lei, Y. Li, W. Shen, M. Zhong, J. Zhang and S. Guo, *Chem. – Eur. J.*, 2022, **28**, e202104380;

(*e*) S. Sisodiya-Amrute, C. Van Stappen, S. Rengshausen, C. Han, A. Sodreau, C. Weidenthaler, S. Tricard, S. DeBeer, B. Chaudret, A. Bordet and W. Leitner, *J. Catal.*, 2022, **407**, 141–148; (*f*) Z.-B. Lin, B.-J. Zeng, S.-M. Wu, L.-Y. Wang, L. Wu, X. Wu, Y. Tian, G.-G. Chang, G. Tian, L. Shen and X.-Y. Yang, *ChemCatChem*, 2024, **16**, e202400656; (*g*) Y. Tang, H. Wang, C. Guo, Z. Yang, T. Zhao, J. Liu, Y. Jiang, W. Wang, Q. Zhang, D. Wu, Y. Zhao, X.-D. Wen and F. Wang, *ACS Nano*, 2024, **18**, 11449–11461; (*h*) Y. Jin, Y. Zhang, J. Gu, Y. Ding, S. Wei, Y. Yang, Y. Dai and X. Gao, *Int. J. Hydrogen Energy*, 2024, **53**, 622–632; (*i*) X. Yu, L. Lin, C. Pei, S. Ji, Y. Sun, Y. Wang, J. K. Kim, H. S. Park and H. Pang, *Chem. – Eur. J.*, 2024, **30**, e202303524.

35 K. Philippot and B. Chaudret, in *Comprehensive Organometallic Chemistry III*, ed. R. H. Crabtree and M. P. Mingos, Elsevier, 2007, vol. 12, ch. 12-03, pp. 71–99.

36 (*a*) P. Lara, O. Rivada-Wheelaghan, S. Conejero, R. Poteau, K. Philippot and B. Chaudret, *Angew. Chem., Int. Ed.*, 2011, **50**, 12080–12084; (*b*) P. Lara, L. N. Martínez-Prieto, M. Roselló-Merino, C. Richter, F. Glorius, S. Conejero, K. Philippot and B. Chaudret, *NanoSO*, 2016, **6**, 39–45.

37 E. A. Owen and E. W. Roberts, *Z. Kristallogr. – Cryst. Mater.*, 1937, **96**, 497–498.

38 R. W. G. Wyckoff, *Crystal Structures*, Interscience Publishers, New York, NY, 2nd edn, 1963, vol. 1, pp. 7–83.

39 (*a*) T. Mathew, S. Shylesh, B. M. Devassy, M. Vijayaraj, C. V. V. Satyanarayana, B. S. Rao and C. S. Gopinath, *Appl. Catal., A*, 2004, **273**, 35–45; (*b*) J. Yang, H. Liu, W. N. Martens and R. L. Frost, *J. Phys. Chem. C*, 2010, **114**, 111–119.

40 M. A. Ernst and W. G. Sloof, *Surf. Interface Anal.*, 2008, **40**, 334–337.

41 (*a*) N. Chakroune, G. Viau, S. Ammar, L. Poul, D. Veautier, M. M. Chehimi, C. Mangeney, F. Villain and F. Fièvet, *Langmuir*, 2005, **21**, 6788–6796; (*b*) D. J. Morgan, *Surf. Interface Anal.*, 2015, **47**, 1072–1079; (*c*) P. Molinillo, B. Lacroix, F. Vattier, N. Rendón, A. Suárez and P. Lara, *Chem. Commun.*, 2022, **58**, 7176–7179.

42 (*a*) A. Rühling, K. Schaepe, L. Rakers, B. Vonhören, P. Tegeder, B. J. Ravoo and F. Glorius, *Angew. Chem., Int. Ed.*, 2016, **55**, 5856–5860; (*b*) M. R. Narouz, C.-H. Li, A. Nazemi and C. M. Crudden, *Langmuir*, 2017, **33**, 14211–14219; (*c*) N. Bridonneau, L. Hippolyte, D. Mercier, D. Portehault, M. Desage-El Murr, P. Marcus, L. Fensterbank, C. Chanéac and F. Ribot, *Dalton Trans.*, 2018, **47**, 6850–6859.

43 X. Bantrei and S. P. Nolan, *Nat. Protoc.*, 2011, **6**, 69–77.

44 C. Pertici, G. Vitulli, W. C. Spink and M. D. Rausch, *Inorg. Synth.*, 1984, **22**, 176–181.

45 S. Otsuka and M. Rossi, *J. Chem. Soc. A*, 1968, 2630–2633.